Mallor, F., Sanmiguel Vila, C., Ianiro, A. & Discetti, S. (2018). Wall-mounted perforated cubes in a boundary layer: Local heat transfer enhancement and control. *International Journal of Heat and Mass Transfer*, vol. 117, pp. 498–507.

DOI: 10.1016/j.ijheatmasstransfer.2017.10.027

Wall-mounted perforated cubes in a boundary layer: local heat transfer enhancement and control

Fermin Mallor, Carlos Sanmiguel Vila, Andrea Ianiro, Stefano Discetti*

Aerospace Engineering Group, Universidad Carlos III de Madrid, Avenida de la Universidad, 30, 28911, Leganes, Spain

Abstract

A passive convective heat transfer enhancement device based on perforated obstacles is proposed. The perforation crosses the obstacle from the flow-facing side to the rear side. In this configuration a jet is delivered from the obstacle perforation, thus changing the topology of the wake behind the obstacle. Measurements of the convective heat transfer over a flat plate equipped with perforated wall-mounted cubes are carried out using infrared thermography. Flow fields measurements are performed with Particle Image Velocimetry to address the effect of the perforation (and of the jet issuing from it) on the wake topology, and on the heat transfer distribution. A modal analysis is carried out with Proper Orthogonal Decomposition to extract the coherent structures organization and the modifications induced by the perforation of the obstacle. When comparing the results of the perforated cubes with those of a solid cube, it can be observed that perforated obstacles offer a simple solution to obtain a localized increase of the convective heat transfer when the perforation crosses the obstacle creating a jet directed towards the wall. This is obtained at the expenses of a reduced space-averaged heat transfer rate due to a 'lift-up' of the recirculation bubble past the obstacle, which postpones the flow reattachment and reduces the velocity of the reattaching flow. Nevertheless, in case of large perforation angles (thus jet issuing with larger angle with respect to the streamwise direction) this penalty is significantly reduced, providing a local gain in terms of heat transfer rate with almost the same overall heat transfer performances as a solid obstacle.

Keywords: boundary layers, wall roughness, heat transfer enhancement, IR thermography, PIV

1. Introduction

The need of cooling objects in compact spaces is fostering the development of advanced heat transfer enhancement strategies since decades. In several fields, such as electronic packaging and turbomachinery, the cooling capabilities are a technology driving factor (see, e.g.[1, 2]).

A common solution to enhance the convective heat transfer of a main flow parallel to a wall consists of using vortex generators. The techniques employed to develop such vortices can be bundled into two main groups, according to the definition by Webb [3]: active and passive heat transfer enhancement methods. Active heat transfer augmentation refers to mechanisms in which external power is required. Some common examples are surface or fluid vibration or flow injection. On the other hand, passive methods do not require any external source of power: special surface geometries interact 'passively' with the flow, enhancing the convective heat transfer by promoting the formation of secondary flow structures. There is a wide range of passive cooling methods; some of the most frequently used ones are extended surfaces (such as plain fins), swirl flow devices or roughness elements. Even though active techniques allow for a more effective heat transfer enhancement control, their power requirement and complexity, compared to passive ones [4], makes the latter still very appealing for industrial applications such as turbomachinery cooling.

The inclusion of obstacles and roughness elements is widely used in industrial applications, both due to the increased surface for heat transfer by convection and for the generation of secondary flow structures. The effect on the heat transfer enhancement produced by obstacles with different geometries such as cubes, cylinders, diamonds and semi-spheres was studied by Chyu and Natarajan [5]. The flow around the different obstacles is characterized upstream by a horseshoe vortex, with two legs extending downstream on each side of it. Downstream of the obstacle the values of the Nusselt number are lower, due to the formation of a recirculation region immediately downstream of the obstacle, followed by the reattachment of an impinging flow referred to as arch-shaped vortex. In [5], the authors conclude that the cube geometry provides the highest enhancement upstream of the obstacle, which is due to the presence of a strong secondary vortex embedded underneath the primary horseshoe vortex. However, downstream of the cube the augmentation is lower than in other configurations (such as the cylindrical or the pyramidal roughness elements). This is due to the flow

*Corresponding author
Email address: sdiscett@ing.uc3m.es (Stefano Discetti)

separation, which leads to a strong recirculation zone immediately downstream of the cube, as well as to the weaker arch-shaped vortex formed downstream of the cube. The region downstream of the cube is characterized by a recirculation zone with relatively lower heat transfer enhancement, followed by the reattachment region. The reattachment of the separated flow from the top surface occurs at a distance of about 2 cube side lengths from the trailing edge of the obstacle, increasing the local Nusselt number Nu, as found by Nakamura et al. [6]. Quite similar results are reported for wall-mounted cylinders by Giordano et al. [7] who showed that the lenght of the separation region is weakly dependent on the cylinder aspect ratio.

In this work, perforated cubes will be used to improve the convective heat transfer augmentation capabilities of a simple cubic obstacle. The concept of perforated roughness elements or obstacles is common in the industry: perforated fins, for example, have been found to be more efficient than solid ones as they not only reduce the flow blockage but also enhance the convective heat transfer [8]. In essence, square section ribs can be idealized as infinite cubes, in which the spanwise dimension is much larger than the other two. Therefore, a better understanding on the mechanics of the passive heat transfer enhancement using a cube as an obstacle can lead to better and more efficient design for state-of-art cooling systems.

Perforating the cube has two main advantages from the viewpoint of heat transfer augmentation. The first advantage is the expected reduction of the negative impact of the recirculation zone on the convection; additionally, the maximum Nusselt number attained is expected to be increased with respect to that of the solid cube configuration due to ejection of fluid through the obstacle. The latter is due to the accelerated flow passing through the hole which, if properly shaped, can act locally as an impinging jet in the wall region immediately past the obstacle. The perforation geometry can be used to tune the distance from the trailing edge of the obstacle at which the maximum Nu is attained in the downstream region by means of varying the angle of the jet. Moreover, the Nusselt number maximum is dependent on the distance between the nozzle and the surface [9, 10], hence, different perforation configurations can result in different Nusselt number distributions. The assessment of the potential of tuning the local maxima of the Nusselt number can open the door for possible new configurations of cube arrays which may improve the present configurations [11].

Jets are usually considered as an active heat transfer enhancement method [3], and they are widely used as cooling mechanisms in industrial applications such as gas turbines [1]. However, in this case no external power is required as the jet is passively formed due to the difference in pressure between the front face and the recirculation zone where the jet is exiting out of the perforation in the cube. Therefore, the beneficial heat transfer aspects of impinging jets are attained without introducing any other momentum source into the cooling mechanism.

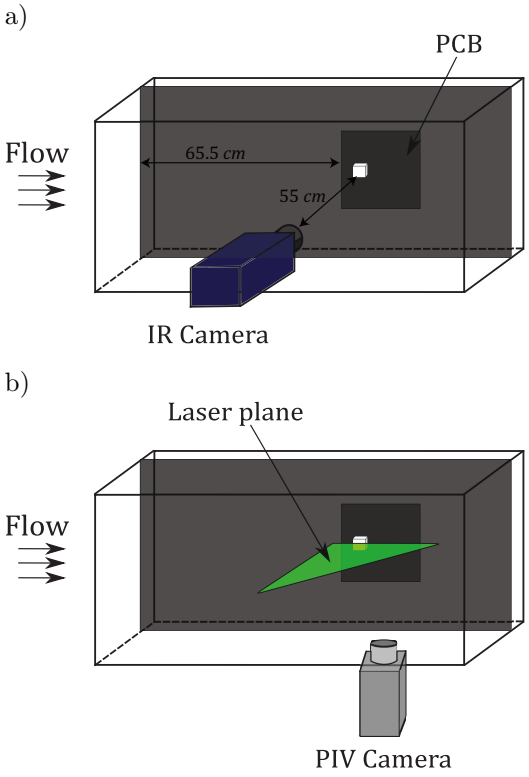

Figure 1: Sketch of the experimental setup: a) IR setup for heat transfer measurements, b) PIV experimental arrangement. IR and PIV measurements were not performed simultaneously.

In order to address the heat transfer capabilites of perforated obstacles, experiments are carried out with Infrared (IR) thermography [12]. Additionally, Particle Image Velocimetry (PIV, [13]) measurements are performed to characterize the flow field features related with the heat transfer enhancement. The methodology and the experimental setup are described in Sec.2. Proper Orthogonal Decomposition (POD, [14]) is used to provide a modal decomposition of the flow field. The results are discussed in Sec.3. Finally, the conclusions are drawn.

2. Methodology

The experiments were carried out in the Göttingen type wind tunnel of the Aerospace Engineering Group at the Universidad Carlos III de Madrid. The wind tunnel has a square test section of 0.4 m x 0.4 m with a length of 1.5 m; it is capable of reaching a maximum speed of 20 m/s with a streamwise turbulence intensity below 1% of the freestream velocity. Both IR thermography and PIV measurements were performed in this work; the experimental setups are sketched in Figure 1.

A splitter plate with a thickness of 10 mm and located at a distance of 0.1 m from the wind tunnel floor was used in the present experimental campaign. In order to obtain a fully developed turbulent boundary layer, a turbulator strip with a height of a 2.4 mm was placed 75 mm downstream of the leading edge. The boundary layer thick-

Table 1: Perforation geometries defined by their non-dimensional inlet (z_{in}/L) and outlet height (z_{out}/L)

Configuration	Baseline	1	2	3	4	5	6	7	8	9
z_{in}/L	-	0.25	0.25	0.25	0.50	0.50	0.50	0.75	0.75	0.75
z_{out}/L	-	0.25	0.50	0.75	0.25	0.50	0.75	0.25	0.50	0.75

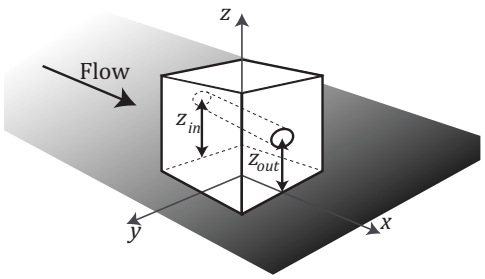

Figure 2: Sketch of the wall mounted perforated cube.

ness δ_{99} (here defined as the position at which 99% of the freestream speed is attained) on the plate without cubes was characterized using PIV and was determined to be of 4.4 cm at the point were the cubes were placed. The diagnostic plot approach was used to assess that the boundary layer approaching the obstacles is not reminiscent of the inflow conditions [15].

The perforated obstacles, sketched in Figure 2, have a base cubical shape with a 10 mm side length L. Hence, their height is approximately a quarter of the local boundary layer thickness ($L/\delta_{99} \approx 0.23$). A single cube was mounted over the printed circuit board (PCB), parallel to the incoming flow.A 90^o bracket was used together with a level when placing the cube in order to ensure a 0^o angle of attack. The solid cube is considered as a baseline configuration to compare the performances of the perforated cubes. Nine different straight perforations, described in Table 1, were analyzed: inlet and outlet exit perforations of 2.5 mm diameter were performed at locations z_{in} and z_{out} equal to $0.25L$, $0.5L$ and $0.75L$, respectively. The perforated cubes have been manufactured by means of a ZCORP 650 3D Printer.

The free stream velocity U_∞ is set to 7.2 m/s for all the cases studied here. This allowed to obtain a local Reynolds number (Re) over the cube equal to 4600 ($Re = U_\infty L/\nu$, where ν is the fluid kinematic viscosity).

A PCB as the one used in [16] is flash-mounted into the flat plate at a distance of 655 mm downstream of the leading edge. The obstacle is located at 50 mm downstream of the upstream edge of the PCB. The PCB is glued to the plate at its edges. There is a thin air gap of 2 mm between the rear part of the circuit substrate and the plate. The PCB has a nominal resistance of 25.5 Ω, a circuit area A_{PCB} of 150 x 150 mm^2 and a thickness of 0.5 mm. A stabilized power supply is used to provide a constant voltage V and current I, which allow to have a constant heat flux due to the Joule effect ($q''_j = VI/A_{PCB}$); then the PCB is cooled by convective heat transfer. In order to obtain the Nusselt number distribution, the convective heat transfer coefficient (h, Equation 1) is estimated through an energy balance, modeling the PCB as a *heated thin foil* sensor [12]:

$$h = \frac{q''_j - q''_r - q''_k}{T_w - T_{aw}}; \tag{1}$$

where T_w is the surface temperature of the PCB, T_{aw} is the adiabatic wall temperature, q''_r is the radiation heat flux and q''_k is the tangential conduction flux through the PCB. Heat flux losses on the rear side of the PCB were minimized thanks to the presence of the thin air gap between the PCB and the plate. These losses due to natural convection within the 2 mm deep cavity were estimated to be below 1% of the convetive heat transfer using correlations for natural convection into rectangular cavities [17]. Natural convection losses on the flow-facing side were neglected since $Gr/Re^2 << 1$ (with $Gr = g\beta(T_w - T_{aw})L^3/\nu^2$ is the Grashoff number, being β the volumetric thermal expansion coefficient and g the gravity acceleration). The radiative heat flux is estimated under the assumption that the environment behaves as a blackbody with temperature equal to the free stream one T_∞.

$$q''_r = \sigma\varepsilon(T_w^4 - T_\infty^4) \tag{2}$$

where σ is the Stefan-Boltzmann's constant and ε is the emissivity of the PCB surface.

Tangential conduction losses through the plate are found to be very small (below 2%) and are estimated according to Equation 3.

$$q''_k = kt\left(\frac{\delta^2 T}{\delta x^2} + \frac{\delta^2 T}{\delta y^2}\right) \tag{3}$$

where k and t are the thermal conductivity and the thickness of the printed circuit board, respectively.

In order to estimate the convective heat transfer coefficient from Equation 1, the surface temperature distribution is required. The temperature measurements are performed with a FLIR SC4000 IR camera (320 × 256 focal plane array elements, noise equivalent temperature difference equal to $20mK$), capturing images at a frequency of 10 Hz with a spatial resolution of 18 $pixels/L$. One of the lateral walls of the test section was modified to provide optical access through a CaF_2 window. In order to improve the accuracy of IR measurements the PCB is coated with a thin layer of high-emissivity paint, with ϵ equal to 0.95. The value of $T_w - T_{aw}$ was computed from two different measurement runs, and the typical value of ΔT

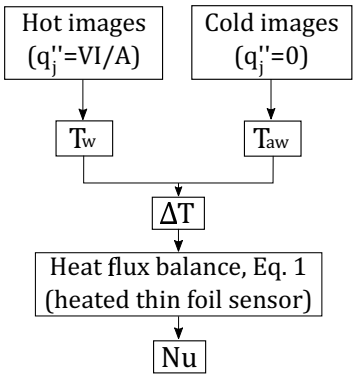

Figure 3: Flowchart of the experimental procedure followed to determine Nu from the IR measurements.

Table 2: Table of uncertainties

Parameter	**Uncertainty**
T_w	0.1 K
T_{aw}	0.1 K
T_∞	0.1 K
A_{PCB}	0.1 %
L	0.1 %
I	0.2 %
V	0.2 %
ϵ	1 %
k_{air}	0.2 %
q''_k	10 %

was determined to be 25 K. T_{aw} is obtained as the mean of 1000 images acquired with $q''_j = 0$; T_w is the mean of 3000 images acquired with the power supply turned on. The flowchart of the procedure to calculate the convective heat transfer coefficient is sketched in Figure 3. The convective heat transfer coefficient distribution is expressed in non-dimensional form in terms of Nusselt number ($Nu = hL/k_{air}$). The experimental uncertainties associated with the measurements were determined through an approach based on a Monte Carlo simulation [18], assuming random errors using the uncertainty values reported in Table 2. The uncertainty on the local Nu is found to be of $\pm 4.4\%$. It has to be highlighted here that this uncertainty includes both random and bias error sources. Bias error sources are in common amongst all the measurements performed with the same setup; consequently it is reasonable to assume a smaller uncertainty when estimating the differences between the results from several experiments (from the current setup). The accuracy of the Nu values measured was checked by comparing them to those obtained by Nakamura et al. [6] at matched Reynolds number, observing a good agreement in the results for the solid cube. The small discrepancies (within 10%) can be addressed to the different L/δ_{99} (equal to about 2/3 in [6], against 0.23 in this study).

The flow fields of the baseline configuration, and for the cubes with holes with inlet and outlet location at $z_{in}/L =$ 0.50 - $z_{out}/L = 0.25$ and $z_{in}/L = 0.75$ - $z_{out}/L = 0.25$, respectively, have been investigated with PIV. The measurements have been performed in the plane $y = 0$ as sketched in Figure 1 b). The experimental setup is essentially the same as that described in [19]. A dual cavity Nd:Yag Quantel Evergreen laser is used in order to illuminate the Di-Ethyl-Hexyl-Sebacate seeding particles. The recording device is an Andor sCMOS camera, equipped with a lens with 100 mm focal length and using an $f/\#$ number equal to 11. Images were recorded with a spatial resolution of 48 $pixels/mm$. Sets of 1000 images have been captured for the 3 test cases. The raw images were preprocessed to remove the background due to the strong reflections using the eigenbackground removal procedure proposed in [20]. The PIV processing to calculate the velocity fields is performed using a custom-made multipass image deformation algorithm [21], implemented by the Thermo-Fluid Dynamics Group of the University of Naples Federico II. The algorithm includes advanced interpolation schemes and weighting windows to improve the spatial resolution and precision of the process [22, 23]. The PIV interrogation process had a final interrogation window size of 64 pixels with 75% overlap resulting in 30 vectors/L.

2.1. POD analysis

A Proper Orthogonal Decomposition analysis is carried out in order to extract information on the coherent turbulent structures in the wake of the obstacles. The POD modes are sorted in terms of their contribution to the total turbulent kinetic energy, consequently allowing to estimate the relative importance of coherent structures in the flow. In particular, the snapshot method [24] has been used for the purpose of the present study.

The POD procedure is briefly outlined in the following lines. For a detailed description, please refer to [14, 25]. A flow field F is decomposed into a time averaged component $\bar{F}(x)$ and a fluctuating component $f(x,t)$:

$$F(x,t) = \bar{F}(x) + f(x,t) \tag{4}$$

where F can be referred, without any loss of generality to the streamwise component U of the velocity or to the in-plane perpendicular velocity component V. Lower case letters indicate fluctuations, while upper case letters with overbars indicate the average field. The maps of the fluctuating velocity fields (having n_p points) have to be rearranged into snapshot vectors $\underline{u}(t)$ and $\underline{v}(t)$ (of length n_p). The available n_t snapshot vectors can be further rearranged in snapshot matrices $\underline{\underline{\mathcal{U}}}$ and $\underline{\underline{\mathcal{V}}}$ whose rows are the n_t snapshot vectors.

The temporal correlation matrix is formed as follows:

$$\underline{\underline{\mathcal{C}}} = \underline{\underline{\mathcal{U}}}\,\underline{\underline{\mathcal{U}}}' + \underline{\underline{\mathcal{V}}}\,\underline{\underline{\mathcal{V}}}' \tag{5}$$

with the apex $'$ indicating the matrix transpose. Solving the eigenvalue problem of the correlation matrix $\underline{\underline{\mathcal{C}}}$ allows to extract its left and right eigenvectors and its eigenvalues.

$$\underline{\underline{\mathcal{C}}} = \underline{\underline{\Psi}}\,\underline{\underline{\Lambda}}\,\underline{\underline{\Psi}}' \tag{6}$$

The eigenvectors of $\underline{\underline{\mathcal{C}}}$ are a basis in the n_t vector space, each one associated to a certain turbulent kinetic energy (equal to the corresponding diagonal element of $\underline{\underline{\Lambda}}$). The left eigenvectors of $\underline{\underline{\mathcal{C}}}$ can be used to project the snapshot matrices $\underline{\underline{\mathcal{U}}}$ and $\underline{\underline{\mathcal{V}}}$, obtaining the spatial modes of streamwise and wall-normal velocity components.

3. Results

3.1. Perforation geometry effect on Nu

The Nusselt number distribution in the wake of the obstacles is presented in the form of contour maps in Figure 4. In all the tested configurations the footprint of the horseshoe vortex upstream of the obstacle is clearly visible as a region with strong local heat transfer rate. The heat transfer peak is reduced in case of perforated obstacles with small perforation height (see for instance the three cases with $z_{in}/L = 0.25$), while it converges to the value of the single cubes as the distance of the hole from the wall is increased.

A protracted wake region downstream of the obstacle with higher heat transfer rate (if compared to the undisturbed boundary layer) is observed. Comparing the different perforation configurations to the baseline case (solid cube with no perforation), it is clear that the configurations in which the perforation creates an impinging jet increase the maximum Nu encountered downstream of the obstacle. Such configurations correspond to those in which the exit height of the perforation is lower than the inlet one; namely configurations 4, 7 and 8.

The maximum Nusselt number is affected by the distance traveled by the fluid from the exit of the perforation, agreeing with the well-known behaviour of impinging jets [9, 10]. The values of the maximum Nusselt number attained in all the tested configuration are reported in Table 3. The relative improvement with respect to the baseline configuration shows that the configurations 4 and 7 are the most performing in terms of local maximum Nusselt number. As expected, the highest Nu_{max} downstream is encountered in case 7 ($z_{in}/L = 0.75$ - $z_{out}/L = 0.25$) due to the fact that this configuration has not only the lowest exit height available, but also the steepest perforation angle (26.5^o). This configuration determines a strong local peak of the Nusselt number.

In order to illustrate the previously mentioned correlation between exit height and distance traveled by the jet with the heat transfer augmentation, it is interesting to compare the configurations 4 and 8 ($z_{in}/L = 0.50$ - $z_{out}/L = 0.25$ and $z_{in}/L = 0.75$ - $z_{out}/L = 0.50$, respectively). The latter reaches a maximum Nusselt number of 26.2 at around $x/L = 0.5$ from the downstream face of the cube, whereas the former reaches $Nu = 27.4$. Both configurations have the same perforation angle of 14^o, but the different height of the obstacle outflow determines a shorter distance to the impingement point for configuration 4 ($z_{in}/L = 0.50$ - $z_{out}/L = 0.25$). For configurations 4 and 8, the corresponding impingement point is located at about 4 diameters and 8 diameters from the nozzle exit, respectively. For turbulent wall-normal impinging jets, the jet arrival velocity is larger for the case of a nozzle to plate distance of 4 diameters than at 8 diameters while the stagnation point Nusselt number depends on the turbulence intensity in the jet [9, 10]. In case of large turbulence intensity within the jet, the heat transfer rate tends to be larger at smaller nozzle to plate distances (see e.g. the jets with fractal grids by [26]).This consideration, in general, should not be straightforwardly applied to the jet issued from the perforation, which has $Re \approx o(1000)$. Additionally, the configuration here is quite different (the jets are issuing in angled impingement configuration, and are delivered within a recirculation bubble). Considering that the inflow is immersed in a turbulent boundary layer, the jet issued from the perforation is likely to experience strong velocity fluctuations in time. This picture is further substantiated by the velocity field measurements, which will be discussed in Sec. 3.2. The observed overall behaviour thus seems compatible with the trend reported in the literature for jets with high incoming turbulence intensity.

Table 3: Local downstream Nu_{max} values for each configuration, and relative improvement in percentage with respect to the baseline case.

Configuration	Nu_{max}	
Baseline	**26.2**	–
1	23.9	−8.8%
2	24.9	−8.8%
3	24.4	−5.0%
4	**27.4**	4.6%
5	24.3	−7.3%
6	24.0	−8.4%
7	**32.5**	24.0%
8	26.2	0.0%
9	24.5	−6.5%

In order to assess the overall performances of each of the configurations, the convective heat transfer rate was averaged over 4 different regions for each of the configurations (as sketched in Figure 5). The schematic also includes the typical thermal footprint observed in Figure 4 in order to provide a straightforward interpretation of the meaning of the cooling performances in each of these regions. The integration areas span from $y/L = (-1.5, 1.5)$ (where y is the spanwise coordinate) and extend in the streamwise direction from the trailing edge of the obstacle up to 4 heights behind it, in steps of one height. The results are reported in Table 4.

The solid cube has overall the best averaged convective heat transfer capabilities. Among the perforated cubes, the configurations 4 and 7 approach similar averaged values, as the reduction in the mean Nu is only by approximately 8.4% and 3% respectively in the region spanning from the trailing edge of the obstacle up to 3 heights be-

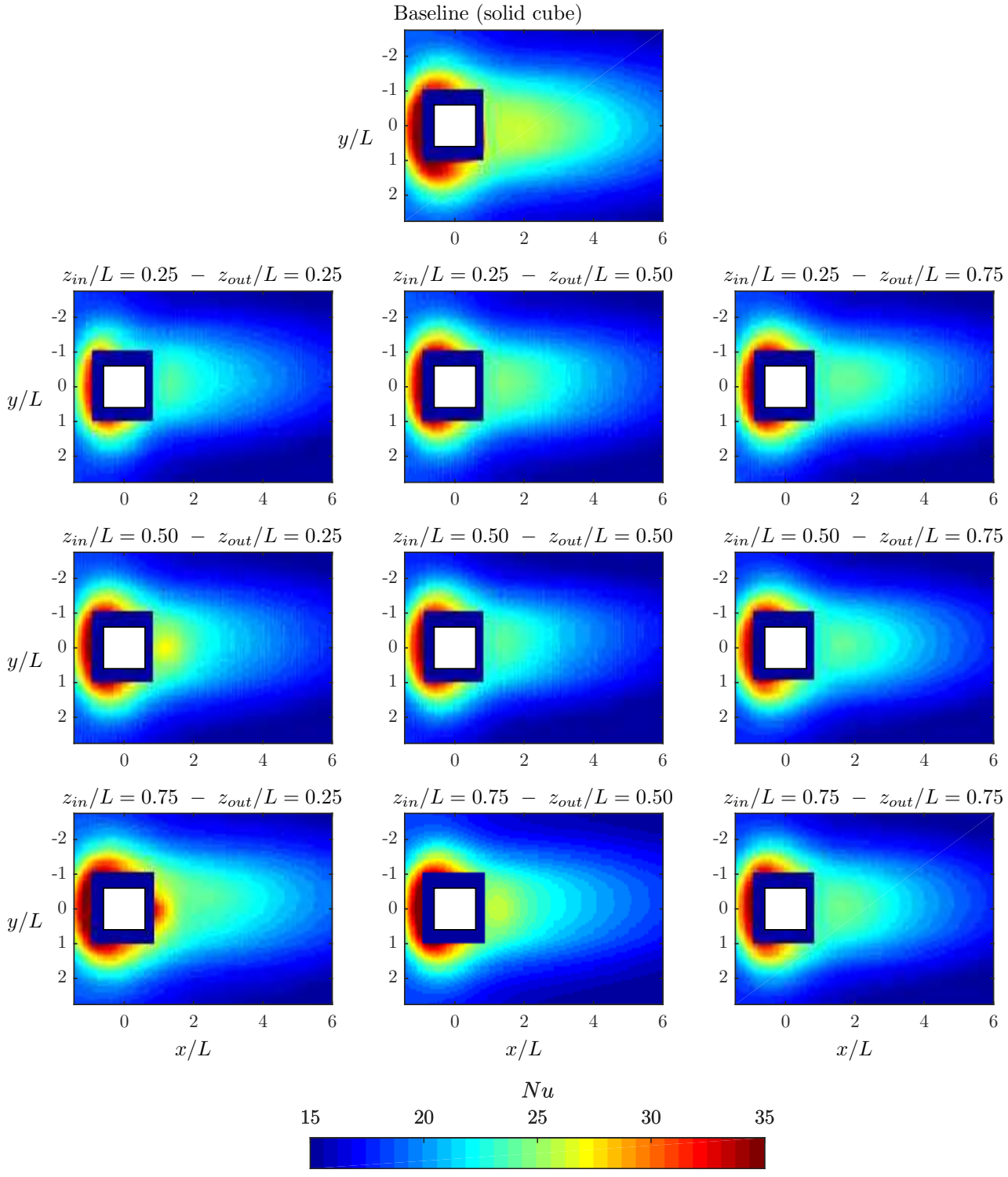

Figure 4: Nusselt number contour maps on the wall with the different obstacle configurations. The cubes planform is shown in white color. Areas around the cube in which the heat transfer measurements are not reliable due to the cube presence (spurious tangential conduction, poor image quality) are blanked in blue color.

hind it, or by 6.1% and 1.3% if a region of only 2 heights is considered. The configuration 7, $z_{in}/L = 0.75$ - $z_{out}/L = 0.25$ reaches larger averaged Nusselt number in the region up to 1 heights past the cube than the solid cube case.

The Nusselt number spatial distributions allow to identify the changes introduced by the jet issued from the perforation of the obstacles, and the relative improvements in terms of heat transfer enhancement when compared to

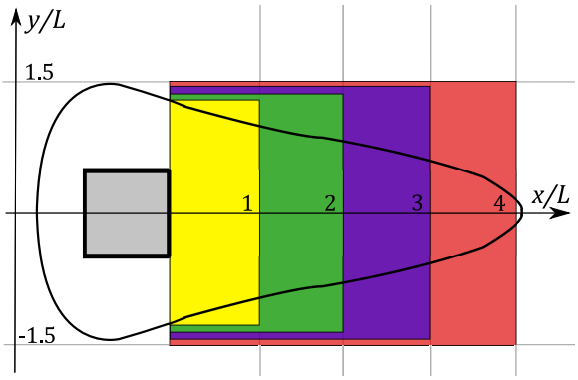

Figure 5: Regions of area-average of Nu. A schematic view of the typical footprint of the obstacle wake is included for reference.

Table 4: Average Nu downstream of the obstacles

Region \Cube Config.	**Baseline**	**1**	**2**	**3**	**4**	**5**	**6**	**7**	**8**	**9**
$\bar{Nu}$ from T.E. to $x/L = 1$	**24.4**	22.0	22.9	22.6	**23.9**	22.4	22.4	**25.5**	23.9	22.8
$\bar{Nu}$ from T.E. to $x/L = 2$	**24.2**	21.6	22.5	22.3	**22.7**	21.8	22.1	**23.9**	23.0	22.5
$\bar{Nu}$ from T.E. to $x/L = 3$	**23.8**	21.1	21.9	21.9	**21.8**	21.2	21.6	**23.1**	22.2	21.9
$\bar{Nu}$ from T.E. to $x/L = 4$	**23.3**	20.6	21.3	21.3	**21.1**	20.5	21.0	**22.5**	21.6	21.3

the baseline case. The impinging jet produced by the perforation has two main effects on the wall convective heat transfer. Firstly, the local minimum of the convective heat transfer corresponding to the recirculation region downstream of the obstacle is eliminated by the presence of the jet, which introduces an increase in flow momentum, enhancing the scalar transport and hence the convective heat transfer. Secondly, as mentioned before, a region of maximum Nu appears around the point of impact of the impinging jet. For the $z_{in}/L = 0.75$ - $z_{out}/L = 0.25$ case, $Nu_{max} = 32.5$ which is a value comparable to those obtained in the upstream region, and represents a 24.0% increase when compared to the solid cube configuration ($Nu_{max} = 26.2$). In the case of the $z_{in}/L = 0.50$ - $z_{out}/L = 0.25$ perforation, the enhancement is smaller (Nu_{max}=27.4, 4.6% increase). The lower increment in Nu for configuration 4 with respect to configuration 7 might be ascribed to the effect of the smaller impingement angle, which results in a smaller wall-normal momentum. This fact becomes apparent if the Nu_{max} region is located for each of the cases: in the former, this region is located immediately downstream of the obstacle, whereas in the second case it is encountered downstream at a distance of half-height from the trailing edge of the cube. These findings pave the way to a passive control of the location of the maximum Nu region by varying the angle of the perforation, effectively changing the point of impingement of the jet. This control ability can have a clear application in electronic packaging [27], since it allows to concentrate the convective heat augmentation capabilities, increasing them, in critical zones where the need for dissipating heat is larger (i.e. at the point where a microchip is located).

3.2. Effect of the jet on the obstacle's wake and convective heat transfer augmentation capabilities

In this section the focus is on three configurations: the solid cube and cases 4 and 7, which have shown to be the most effective configurations in terms of heat transfer capabilities. Figure 6 shows contour maps of the time-average streamwise velocity, U, with superimposed velocity vectors. The velocity vectors have been downsampled by a factor of 3 for clarity. As described by [6], the front face has the highest positive pressure coefficient, whereas the back side of the obstacle has a negative pressure coefficient due to flow separation. This pressure difference drives the flow passing through the cube, which then impinges on the PCB surface. The jet maximum speed is comparable to that of the freestream, thus it has a much larger velocity than the recirculating flow surrounding it. As it travels towards the PCB, the jet mixes with the slower surrounding flow, thus reducing its velocity owing to momentum conservation. This further stresses the need of having a steep angle of perforation in order to minimize the loss of velocity of the impinging jet.

The lower overall averaged Nu of the perforated configurations when compared to the baseline case can also be explained by observing the mean streamwise velocity contour maps. The jet *lifts* the recirculation bubble in the separated region. This has a positive impact in terms of local heat transfer rate due to the presence of the impinging jet instead of a low momentum recirculation region. This explains the higher average Nu obtained in the region extending up to one height behind the obstacle in the case of $z_{in}/L = 0.75$ - $z_{out}/L = 0.25$ (case 7). However, lifting the recirculating bubble has a negative impact on the reattachment of the separated flow passing on top

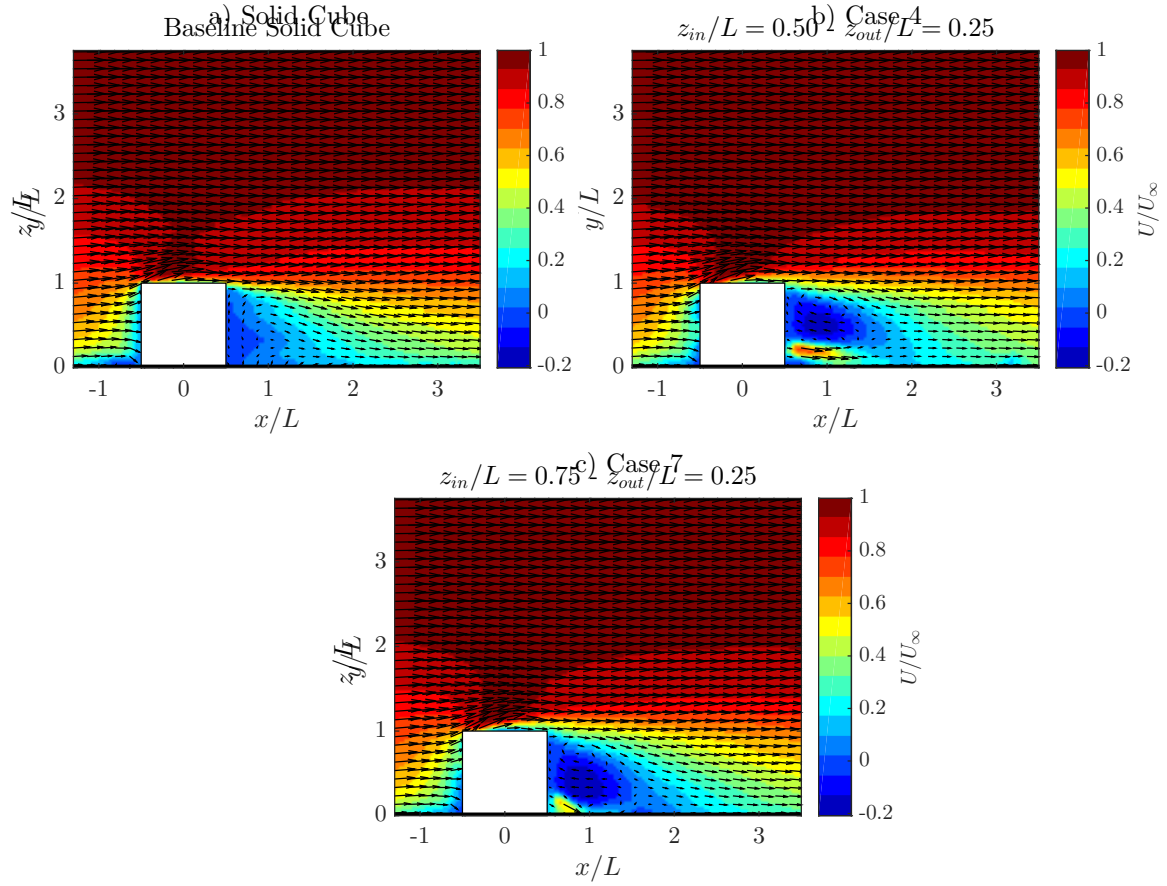

Figure 6: Mean streamwise velocity ($\bar{U}$) field in the $x = 0$ plane obtained using PIV for a) the solid cube, b) Case 4 ($z_{in}/L = 0.50$ - $z_{out}/L = 0.25$) and c) Case 7 ($z_{in}/L = 0.75$ - $z_{out}/L = 0.25$). The arrows represent the mean velocity vectors. For clarity an arrow each 3 grid points is included.

of the obstacle: the reattachment location is indeed postponed further downstream. Consequently, the reattached flow has a lower streamwise velocity than in the solid cube case, thus resulting in a lower average Nu downstream of the obstacle. Comparing the mean velocity fields of cases 4 and 7 it is clear that as the jet comes out at an angle from the obstacle, it is effectively tilting the recirculating bubble. As configuration 7 has a steeper angle, this effect is stronger, thus the flow reattaches more rapidly with respect to case 4. This results in a lower averaged Nu for case 4 downstream of the obstacle when compared to case 7, as it can be checked in Table 4.

Boundary layer statistics have been extracted to further analyze the effect of the perforation of the obstacle on the flow field. The profiles are scaled in outer variables, i.e. using the boundary layer thickness δ_{99} where 99% of the freestream velocity is achieved, indicated with $U_{\delta_{99}}$. The normalized streamwise velocity defect and normal Reynolds stress in four different regions are shown in Figure 7. The wall-normal profiles are obtained after averaging along the streamwise directions in intervals with width equal to one cube height. It is clear that the perforation has negligible effects on the boundary layer upstream of the obstacle. Figure refBLstatsb) shows the increase in the streamwise normal Reynolds stress due to the jet issuing from the obstacle. The jet reduces the velocity defect close to the wall if compared to the solid cube. On the downside, the recirculation bubble is stretchted due to the interaction with the jet. The presence of the jet results in a pressure increase in the region behind the obstacle, reducing the suction responsible of the reattachment of the flow. This result can be further qualitatively explained if comparing the flow behaviour of the backward facing step flow with respect to the wake of a bluff body. The wake is generally characterized by a von Kármán shedding, which has a longer wavelength than the Kelvin-Helmholtz instability characteristic of the separated shear layer of a backward facing step. Clearly this is a simplistic picture, considering that the flow field under investigation is strongly three-dimensional.

The configuration with the steepest jet angle (case 7) has the highest turbulence intensity in this region immediately past the cube. Further downstream, in the areas encompassed between 1 and 3 heights past the obstacle, the streamwise Reynolds stress is smeared out and the velocity defect due to the recirculation bubble protraction is

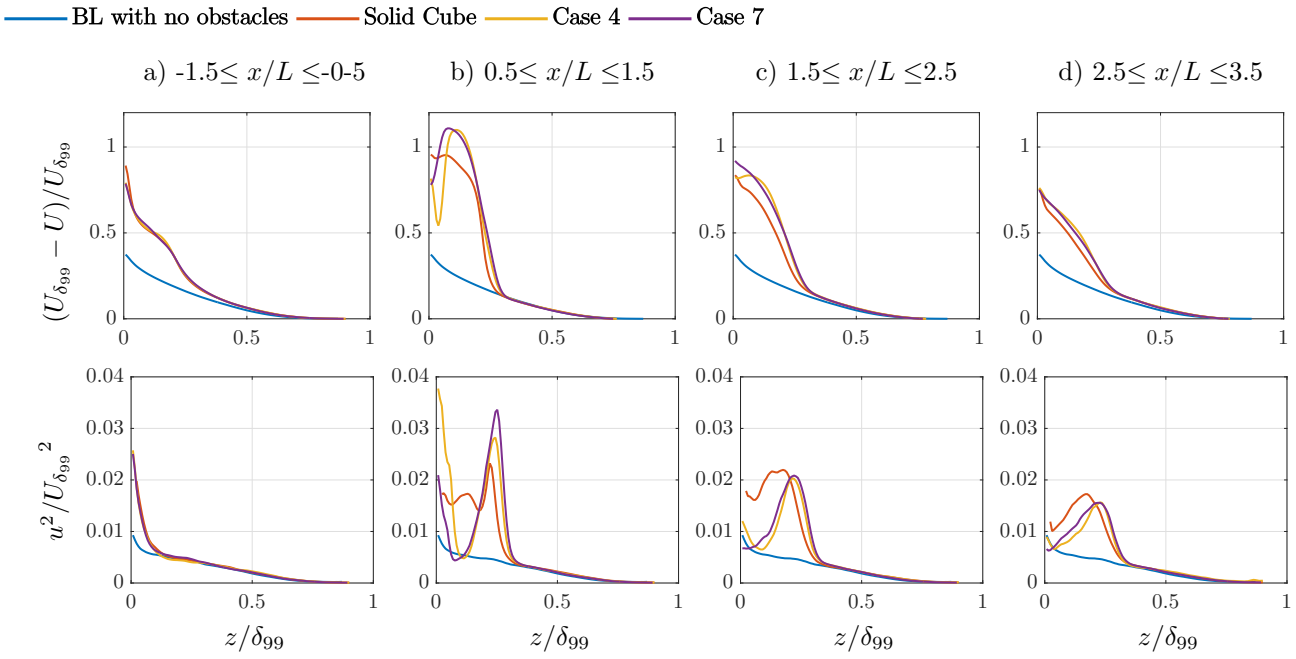

Figure 7: Streamwise averaged wall-normal profiles of velocity defect (top row) and streamwise normal Reynolds stress (bottom row) in the boundary layer upstream of the obstacle (a) and downstream from it (b, c and d). Averaging intervals indicated in the captions.

significantly reduced, thus suggesting a lower drag of perforated cubes. It is interesting to note that the streamwise Reynolds stress peak is slightly reduced in intensity and displaced to a larger distance from the wall when using perforated obstacles. This reduction in turbulence intensity close to the wall is responsible for a lower average Nu in those regions and it is a consequence of the interaction between the jet and the recirculation bubble, which, due to the stretching of the latter, results in a decrease of the impinging velocity of the reattaching flow at the reattachment point, and in a downstream displacement of the reattachment point itself.

The eigenspectrum obtained from the POD analysis is plotted in Figure 8. The singular values represent the contribution of each mode in building the turbulent kinetic energy. The most relevant difference is observed in the first 3 modes; in the case of the solid cube, modes 2 and 3 have a similar energy content, thus providing hints of a strong coupling between these two modes. This is confirmed when observing the spatial modes topology. The first four spatial modes of the streamwise velocity component are shown in Figure 9. The effect of introducing a perforation in the obstacle is quite clear when observing the first mode. This mode accounts for 8% of the total kinetic energy (the next mode relative weight goes down to around 4.5 to 5.4% depending on the case in hand), almost independently on the analyzed case. For the solid cube, this mode is composed by the structure formed by the shear layer and the recirculation zone past the obstacle. Thus, it is clear that the recirculation and the shedding within the shear layer are coupled in this case. In the case of perforated obstacles,

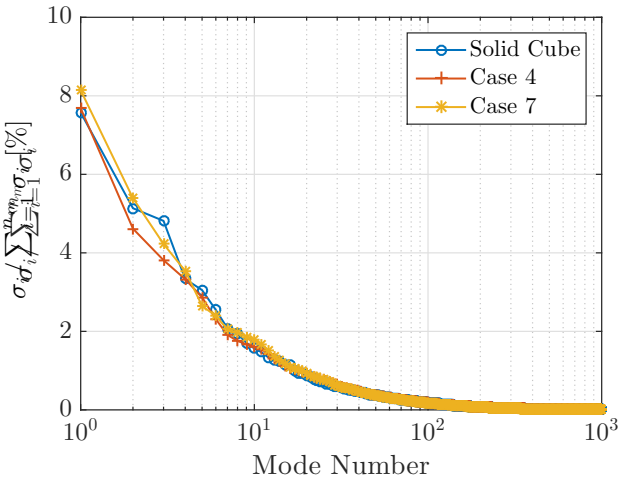

Figure 8: Relative weight of each of the modes for the solid cube, case 4 and case 7.

the shear layer on top of the cube and the recirculation bubble are stretched along the streamwise direction and the jet appears clearly in the first mode, thus supporting the scenario of a strong interaction with the recirculation bubble and the reattaching flow. Moreover, a secondary effect of the jet is also seen in Figure 9: the second and the third mode of the perforated cubes are similar, although referring to structures shifted away from the wall, with respect to the second mode of the solid cube. This mode is a representation of the shedding in the wake of the ob-

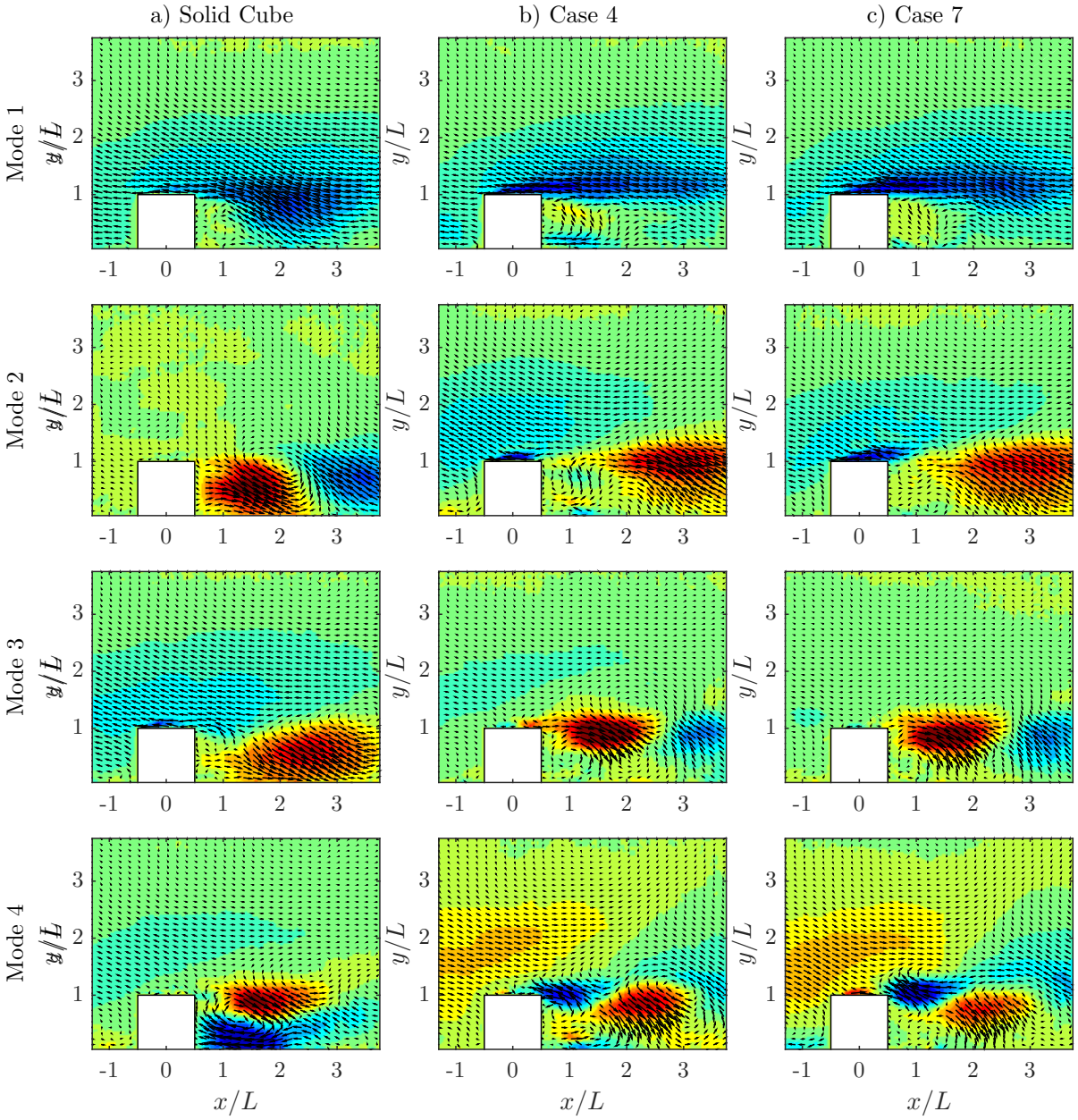

Figure 9: First four spatial modes of the streamwise unsteady velocity component u' obtained using POD for a) the solid cube, b) Case 4 ($z_{in}/L = 0.50$ - $z_{out}/L = 0.25$) and c) Case 7 ($z_{in}/L = 0.75$ - $z_{out}/L = 0.25$). The arrows represent the velocity vectors corresponding to the spatial modes of the streamwise and wall-normal velocity components. For clarity an arrow each 3 grid points is included.

stacles. The wake-generated vortices, however, are lifted away from the wall in the case of the perforated obstacles. Furthermore, their intensity and the domain that is affected by them is reduced due to the presence of the jet. The same holds for the fourth mode which represents a flapping motion of the shed vortices and appears to be influenced by a jet flapping nearby the wall downstream of the perforated cubes.

4. Conclusions

Experimental measurements of the convective heat transfer of wall-mounted cubic obstacles immersed in a turbulent boundary layer have been carried out. Perforated obstacles have been tested to assess the effect of different perforation geometries on the heat transfer and on the flow field organization. The results show that the best heat transfer performances are achieved when the flow passing through the perforation of the obstacles is directed towards the wall, i.e. when the exit height is smaller than the entry height. In this case an impinging jet is created,

which determines a local peak of the heat transfer rate right downstream of the obstacle, as well as an elongation of the recirculation region past of it.

It has been demonstrated that a small distance between the jet issued from the perforation and the impinged surface is desirable, as well as a large impingement angle (as close as possible to the condition of a jet perpendicular to the surface). These two conditions create a zone of maximum Nu very close to the obstacle, reducing the negative effects of the recirculation bubble which is formed behind the solid obstacle. The recirculation bubble is not eliminated by the jet, but simply 'lifted' from the surface. Due to this lifting, the shedding layer created from the separation at the cube's top face reattached further downstream if compared to the solid obstacle, thus resulting in smaller area-averaged heat transfer rate. The impinging angle of the jet plays a key role in this direction. Increasing the impinging angle (i.e. jet closer to be perpendicular to the wall) tilts the recirculating bubble, reducing its streamwise extent and promoting the earlier reattachment of the flow when compared to cases with lower jet angle.

The reduction in terms of average Nusselt number (when compared to the solid cube case) are found to be quite low when using the highest angle and smallest jet-to-wall distance (as small as a 3% reduction in an area spanning up to three heights downstream of the cube). This configuration increased the local maximum Nusselt number by more than 20%, with this value attained at a tunable location behind the cube. This location is indeed dependent on the perforation geometry, hence, allowing for heat transfer enhancement control opportunities: depending on the application, different perforation geometries could be used in order to locally optimize the cooling.

Acknowledgements

Carlos Sanmiguel Vila, Andrea Ianiro and Stefano Discetti have been partially supported by the Grant DPI2016-79401-R funded by the Spanish State Research Agency (SRA) and European Regional Development Fund (ERDF). Fermin Mallor has been partially supported by the fellowship "Beca de colaboracion 2016/17" of the Spanish Ministry of Education.

References

[1] J.-C. Han, S. Dutta, S. Ekkad, Gas turbine heat transfer and cooling technology, CRC Press, 2012.

[2] S. V. Garimella, L. Yeh, T. Persoons, Thermal management challenges in telecommunication systems and data centers, IEEE Transactions on Components, Packaging and Manufacturing Technology 2 (8) (2012) 1307–1316.

[3] R. L. Webb, N. Kim, Enhanced heat transfer, Taylor and Francis, NY.

[4] A. M. Jacobi, R. K. Shah, Heat transfer surface enhancement through the use of longitudinal vortices: A review of recent progress, Experimental Thermal and Fluid Science 11 (3) (1995) 295–309.

[5] M. K. Chyu, V. Natarajan, Heat transfer on the base surface of three-dimensional protruding elements, International Journal of Heat and Mass Transfer 39 (14) (1996) 2925–2935.

[6] H. Nakamura, T. Igarashi, T. Tsutsui, Local heat transfer around a wall-mounted cube in the turbulent boundary layer, International Journal of Heat and Mass Transfer 44 (18) (2001) 3385–3395.

[7] R. Giordano, A. Ianiro, T. Astarita, G. M. Carlomagno, Flow field and heat transfer on the base surface of a finite circular cylinder in crossflow, Applied Thermal Engineering 49 (2012) 79–88.

[8] J. J. Hwang, T. M. Liou, Heat transfer and friction in a low-aspect-ratio rectangular channel with staggered perforated ribs on two opposite walls, Journal of Heat Transfer 117 (4) (1995) 843–850.

[9] K. Jambunathan, E. Lai, M. Moss, B. Button, A review of heat transfer data for single circular jet impingement, International Journal of Heat and Fluid Flow 13 (2) (1992) 106–115.

[10] G. M. Carlomagno, A. Ianiro, Thermo-fluid-dynamics of submerged jets impinging at short nozzle-to-plate distance: a review, Experimental Thermal and Fluid Science 58 (2014) 15–35.

[11] M. K. Chyu, Y. C. Hsing, V. Natarajan, Convective heat transfer of cubic fin arrays in a narrow channel, Journal of Turbomachinery 120 (2) (1998) 362–367.

[12] G. M. Carlomagno, G. Cardone, Infrared thermography for convective heat transfer measurements, Experiments in Fluids 49 (6) (2010) 1187–1218.

[13] J. Westerweel, G. E. Elsinga, R. J. Adrian, Particle image velocimetry for complex and turbulent flows, Annual Review of Fluid Mechanics 45 (2013) 409–436.

[14] P. Holmes, J. L. Lumley, G. Berkooz, C. W. Rowley, Turbulence, coherent structures, dynamical systems and symmetry, Cambridge university press, 2012.

[15] C. Sanmiguel Vila, R. Vinuesa, S. Discetti, A. Ianiro, P. Schlatter, R. Örlü, On the identification of well behaved turbulent boundary layers, Journal of Fluid Mechanics 822 (2017) 109138.

[16] C. Sanmiguel Vila, S. Discetti, G. M. Carlomagno, T. Astarita, A. Ianiro, On the onset of horizontal convection, International Journal of Thermal Sciences 110 (2016) 96–108.

[17] T. L. Bergman, F. P. Incropera, Fundamentals of heat and mass transfer, John Wiley & Sons, 2011.

[18] W. Minkina, S. Dudzik, Infrared thermography: errors and uncertainties, John Wiley & Sons, 2009.

[19] M. Raiola, A. Ianiro, S. Discetti, Wake of tandem cylinders near a wall, Experimental Thermal and Fluid Science 78 (2016) 354–369.

[20] M. Mendez, M. Raiola, A. Masullo, S. Discetti, A. Ianiro, R. Theunissen, J.-M. Buchlin, Pod-based background removal for particle image velocimetry, Experimental Thermal and Fluid Science 80 (2017) 181–192.

[21] F. Scarano, Iterative image deformation methods in piv, Measurement science and technology 13 (1) (2001) R1.

[22] T. Astarita, Analysis of interpolation schemes for image deformation methods in piv: effect of noise on the accuracy and spatial resolution, Experiments in Fluids 40 (6) (2006) 977–987.

[23] T. Astarita, Analysis of weighting windows for image deformation methods in piv, Experiments in Fluids 43 (6) (2007) 859–872.

[24] L. Sirovich, Turbulence and the dynamics of coherent structures. i. coherent structures, Quarterly of Applied Mathematics 45 (3) (1987) 561–571.

[25] G. Berkooz, P. Holmes, J. L. Lumley, The proper orthogonal decomposition in the analysis of turbulent flows, Annual Review of Fluid Mechanics 25 (1) (1993) 539–575.

[26] G. Cafiero, S. Discetti, T. Astarita, Heat transfer enhancement of impinging jets with fractal-generated turbulence, International Journal of Heat and Mass Transfer 75 (2014) 173–183.

[27] F. P. Incropera, Convection heat transfer in electronic equipment cooling, Journal of Heat Transfer 110 (4B) (1988) 1097–1111.